
Article:
Fujii, Shumpei, Usami, Takamasa, Shiratsuchi, Yu et al. (9 more authors) (2022) Giant converse magnetoelectric effect in a multiferroic heterostructure with polycrystalline Co2FeSi. NPG Asia Materials. 43. ISSN 1884-4049

https://doi.org/10.1038/s41427-022-00389-1

Fujii et al. *NPG Asia Materials* (2022)14:43
https://doi.org/10.1038/s41427-022-00389-1

NPG Asia Materials

ARTICLE Open Access

Giant converse magnetoelectric effect in a multiferroic heterostructure with polycrystalline Co_2FeSi

Shumpei Fujii[1], Takamasa Usami[2], Yu Shiratsuchi[2,3], Adam M. Kerrigan[4], Amran Mahfudh Yatmeidhy[5], Shinya Yamada[1,2], Takeshi Kanashima[1], Ryoichi Nakatani[2,3], Vlado K. Lazarov[4], Tamio Oguchi[2], Yoshihiro Gohda[2,5] and Kohei Hamaya[1,2,6]

Abstract

To overcome a bottleneck in spintronic applications such as those of ultralow-power magnetoresistive random-access memory devices, the electric-field control of magnetization vectors in ferromagnetic electrodes has shown much promise. Here, we show the giant converse magnetoelectric (CME) effect in a multiferroic heterostructure consisting of the ferromagnetic Heusler alloy Co_2FeSi and ferroelectric-oxide $Pb(Mg_{1/3}Nb_{2/3})O_3$-$PbTiO_3$ (PMN-PT) for electric-field control of magnetization vectors. Using an in-plane uniaxial magnetic anisotropy of polycrystalline Co_2FeSi film grown on PMN-PT(011), the nonvolatile and repeatable magnetization vector switchings in remanent states are demonstrated. The CME coupling coefficient of the polycrystalline Co_2FeSi/PMN-PT(011) is over 1.0×10^{-5} s/m at room temperature, comparable to those of single-crystalline $Fe_{1-x}Ga_x$/PMN-PT systems. The giant CME effect has been demonstrated by the strain-induced variation in the magnetic anisotropy energy of Co_2FeSi with an $L2_1$-ordered structure. This approach can lead to a new solution to the reduction in the write power in spintronic memory architectures at room temperature.

Introduction

Switching the magnetization vectors via spin transfer torque using an electric current has been utilized as a method of writing information for next-generation spintronic nonvolatile memories such as magnetoresistive random-access memory (MRAM) devices[1–4]. In general, a high electric current density is required to switch the magnetization vectors of ferromagnetic electrodes in magnetic tunnel junctions (MTJs) during the information writing process, and it is a serious bottleneck in the application of spintronic devices. For this problem, several methods for manipulating magnetization vector via an electric field are expected to markedly reduce the power consumption[5]. However, there are limitations on the usage environment of ferromagnetic semiconductors[6,7] and ultrathin ferromagnets[8,9] to control and/or change the magnetization vectors. In practical applications, it is very desirable to switch the magnetization vectors by an electric field without using an assist-magnetic field above room temperature.

The realization of these requirements has been the focus of numerous studies on multiferroic materials[10–13]. For robust operation above room temperature and a wide variety of material selections, artificial ferromagnetic (FM)/ferroelectric (FE) multiferroic heterostructures have been explored because of their potential advantages, such as high operation temperatures[14–24]. In particular, when $Pb(Mg_{1/3}Nb_{2/3})O_3$-$PbTiO_3$ (PMN-PT) was utilized as an FE material, relatively high magnetostriction through the piezostrain and repeatable switching of the remanent magnetization states with a nonvolatile nature were

Correspondence: Kohei Hamaya (hamaya.kohei.es@osaka-u.ac.jp)
[1]Department of Systems Innovation, Graduate School of Engineering Science, Osaka University, 1-3 Machikaneyama, Toyonaka, Osaka 560-8531, Japan
[2]Center for Spintronics Research Network, Graduate School of Engineering Science, Osaka University, 1-3 Machikaneyama, Toyonaka, Osaka 560-8531, Japan
Full list of author information is available at the end of the article

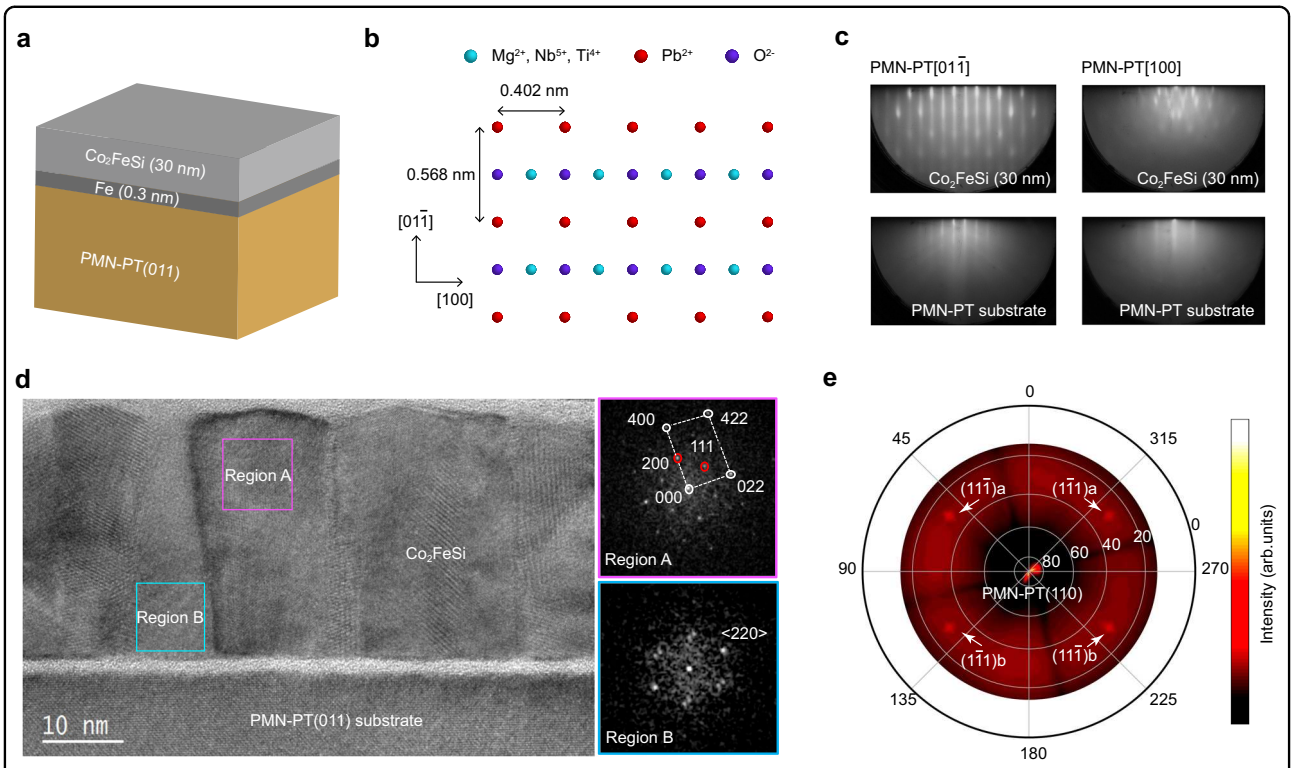

Fig. 1 Growth of Co_2FeSi/PMN-PT(011) heterostructures. a Schematic of the fabricated Co_2FeSi/PMN-PT(011) heterostructure. **b** Atomic arrangements of the (011) plane for the PMN-PT pseudocubic single crystal. **c** RHEED patterns of the Co_2FeSi layer during the growth (top) and the surface of PMN-PT(011) before growth (bottom) along the PMN-PT[01$\bar{1}$] and PMN-PT[100] directions under the observations. **d** HRTEM of the Co_2FeSi/PMN-PT heterostructure near the interface (left) and digital diffractograms measured at region A and region B. **e** XRD pole figure of the $L2_1$-ordered structure for Co_2FeSi on PMN-PT(011).

experimentally observed[25–30]. Recently, nonvolatile switching of the magnetization vector via an electric field was repeatedly demonstrated in MTJs with high magnetoresistance ratios at room temperature[31,32]. By sequentially applying uniaxial stress in FM/PMN-PT systems[33], complete 180° magnetization reversal of FM on PMN-PT and large magnetoresistance (MR) changes can be performed without using an assist-magnetic field, even for MTJs[32]. The combination of the above technique and giant magnetoelectric (ME) coupling coefficients of more than 1.0×10^{-5} s/m are required for future spintronic logic and memory architectures to efficiently switch the magnetization vectors via an electric field[23–25].

With respect to the giant ME coupling coefficients of more than 1.0×10^{-5} s/m, single-crystalline $Fe_{1-x}Ga_x$ alloys grown on PMN-PT are promising materials[34,35], as $Fe_{1-x}Ga_x$ alloys are good magnetostrictive materials for strain sensors, actuators, and energy harvesters[36,37]. However, spin polarization at the Fermi level of $Fe_{1-x}Ga_x$ alloys is less than that of spintronic materials[36]. Thus, high-performance spintronic materials, such as FM half-metals grown on PMN-PT, should be explored to realize magnetization switching with ultralow power consumption[23–25]. Here, we have chosen Co-based Heusler alloys, since they are expected to be half-metallic materials with high Curie temperatures[38–40]. In this work, we focus particularly on Co_2FeSi as an FM material because the $L2_1$-ordered Co_2FeSi has already shown a half-metallic nature[40–42]. We demonstrate giant ME coupling coefficients of more than 1.0×10^{-5} s/m by utilizing high-performance polycrystalline Co_2FeSi films with the $L2_1$-ordered structure on PMN-PT(011). The findings in the present study have the potential to overcome the current bottleneck in spintronic devices.

Results

Polycrystalline Co_2FeSi/PMN-PT(011) heterostructures

We use an FE rhombohedral PMN-PT pseudocubic substrate with a large piezoelectric constant[43]. Unlike in the previous report on PMN-PT(001)[29], the PMN-PT(011) single crystal is chosen because there have been many studies on the electric-field control of the magnetization vector[26–28]. The detailed growth procedure of Co_2FeSi films on PMN-PT(011) is described in the Materials and methods.

A schematic of the Co_2FeSi/PMN-PT(011) heterostructure is shown in Fig. 1a, where a 0.3-nm-thick Fe layer is inserted between Co_2FeSi (30 nm) and PMN-PT(011). This layer was added to improve the crystallinity of the

Co_2FeSi films, since films with poor structural quality are unlikely to have a substantial converse ME (CME) effect[29]. In Fig. 1b, we present a schematic of the atomic arrangements of a (011) plane for the PMN-PT pseudocubic single crystal. An evident difference in the atomic arrangement between PMN-PT[01$\bar{1}$] and PMN-PT[100] crystallographic directions is expected. Prior to the growth of Co_2FeSi films, we confirm that in situ reflection high-energy electron diffraction (RHEED) patterns indicate two different atomic arrangements of the PMN-PT[01$\bar{1}$] and PMN-PT[100] directions, as shown at the bottom of Fig. 1c. During the growth of the Co_2FeSi layers, we can also find a distinct difference in the RHEED patterns of the Co_2FeSi surface between the PMN-PT[01$\bar{1}$] and PMN-PT[100] azimuths in the top of Fig. 1c. The two different RHEED patterns indicate that the growth mode of the Co_2FeSi layer on the (011) surface of PMN-PT is anisotropic.

Figure 1d is a high-resolution transmission electron microscopy (HRTEM) image from a region at the interface that shows the PMN-PT substrate and the Co_2FeSi film. The HRTEM clearly shows that between the substrate and film, an amorphous layer forms during growth, since the in situ RHEED from the substrate shows a well-ordered crystalline PMN-PT(011) surface. The EDX spectra from the amorphous interface layers (not shown here) showed that the amorphous layer in Fig. 1d is an oxide with little Co, Fe or Si. The grown film is polycrystalline with a grain width of 13 ± 4 nm. Co_2FeSi grains are highly textured; hence, the RHEED patterns indicate epitaxial like film growth. The digital diffractograms from the labeled regions of the grains (Fig. 1d) show the grain orientations and the $L2_1$ structure of the Co_2FeSi grains by observing the (111) ordering spots. We also performed nanodiffraction (see Figs. S1 and S2 of Supplementary information[44]) from individual grains that show the preferred grain growth along the [422] and [220] directions, and the results are further confirmed and discussed in the next paragraph.

The structural analysis from the X-ray diffraction (XRD) ω-2θ scan (out-of-plane) for the Co_2FeSi/PMN-PT(011) heterostructure is shown in Fig. S3 of the Supplementary information[44]. Weak diffraction peaks from the (220) and (422) planes were observed in the out-of-plane XRD measurement (Fig. S3a), indicating that the grown Co_2FeSi layer was not a highly oriented structure on PMN-PT(011), consistent with the data shown in Fig. 1d. On the other hand, from the pole figure measurement ($2\theta = 27.55$ degrees) shown in Fig. 1e, we clearly observed {111} diffraction peaks, indicating the presence of the $L2_1$-ordered structure of Co_2FeSi. These results are consistent with the results observed in the HRTEM image and diffractogram shown in Fig. 1d and the results presented in Figs. S1 and S2 of the Supplementary information[44]. From these structural characterizations, we conclude that the grown Co_2FeSi layer is a textured polycrystalline film on PMN-PT(011), in which the polycrystalline Co_2FeSi film includes the high spin polarization $L2_1$-ordered structure [40–42].

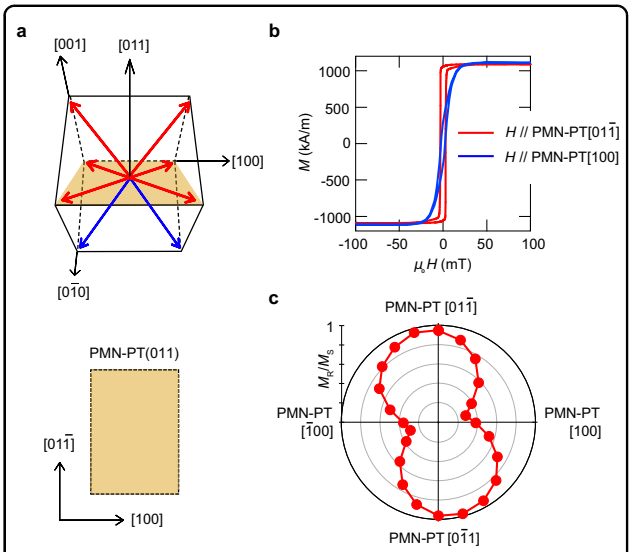

Fig. 2 In-plane uniaxial magnetic anisotropy of a Co_2FeSi/PMN-PT(011) heterostructure. a Schematics of the correlation between spontaneous polarization vectors and crystal orientations of the (011)-oriented PMN-PT substrate. **b** Magnetization hysteresis curves measured at 300 K under H along PMN-PT[01$\bar{1}$] (red) and PMN-PT[100] (blue). **c** A polar plot of the remanent magnetization (M_R) normalized by the saturation magnetization (M_S) at 300 K. In-plane magnetic anisotropy is observed near PMN-PT[01$\bar{1}$].

Initial in-plane uniaxial anisotropy

Prior to the investigation of magnetic properties of the Co_2FeSi/PMN-PT(011) heterostructure, we briefly present the well-known unpoled state of the PMN-PT(011) substrate[21], as schematically shown in Fig. 2a. The spontaneous piezoelectric polarizations of (011) cut PMN-PT lie along the diagonals of the (011) plane and (01$\bar{1}$) plane, as shown in the top section of the figure[21]. In this situation, the (011) plane of the PMN-PT pseudocubic single crystal has a rectangular shape with a long axis along the [01$\bar{1}$] direction, as depicted at the bottom of the figure.

We first measure general magnetic properties of the Co_2FeSi/PMN-PT(011) heterostructure at room temperature. Magnetic-field (H)-dependent magnetization, measured along the PMN-PT[01$\bar{1}$] and PMN-PT[100] crystallographic directions in the film plane, is presented in Fig. 2b. An anisotropic feature of the magnetization curves is present along the two different crystal axes, where the two different RHEED patterns are observed during the growth in Fig. 1c. Because the value of the saturation magnetization (M_S) (1090 ± 30 kA/m) is nearly the same as that in our previous works on Co_2FeSi films[29,42,45], we regard the relatively high M_S value as a consequence of the formation of the $L2_1$-ordered structure. Figure 2c shows a polar plot of the squareness of the

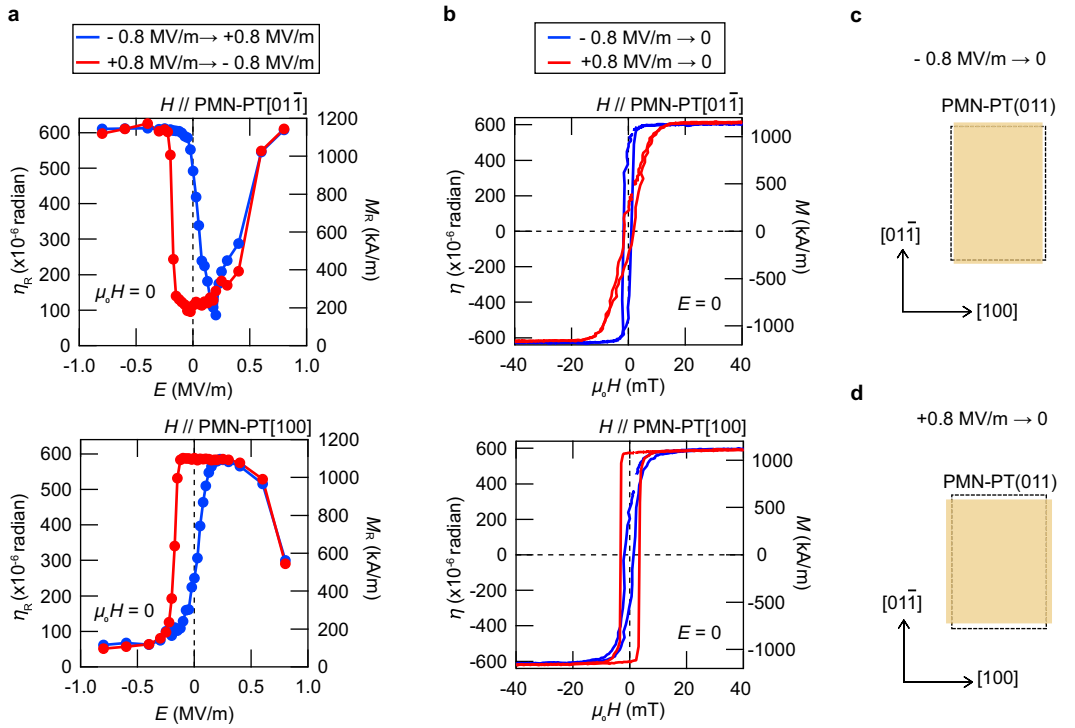

Fig. 3 Converse magnetoelectric effect. a *E*-dependent remanent magnetization measured along PMN-PT[01$\bar{1}$] and PMN-PT[100] at room temperature. The blue and red plots are the up-sweep and down-sweep data, respectively, within an *E* of ±0.8 MV/m. **b** Room-temperature magnetization curves measured along PMN-PT[01$\bar{1}$] and PMN-PT[100] for the two different states at $E = 0$. The blue and red curves were measured after *E* sweeping from −0.8 MV/m to 0 or from +0.8 MV/m to 0, respectively. **c**, **d** Lattice deformation of the (011) plane at $E = 0$ when *E* is changed from −0.8 MV/m to 0 and from +0.8 MV/m to 0, respectively, in the presence of the anisotropic piezostrain of the (011) plane.

magnetization curves, where the remanent magnetization (M_R) is normalized by M_S in various *H* directions in the film plane. In the Co_2FeSi/PMN-PT(011) heterostructure, an evident in-plane uniaxial magnetic anisotropy along the PMN-PT[01$\bar{1}$] with a small off-axis orientation is induced. These features are reproduced for multiple samples. Since the observed uniaxial anisotropy is almost parallel to the long axis of the rectangular shape of the (011) plane of PMN-PT (the bottom of Fig. 2a), the in-plane uniaxial magnetic anisotropy can be understood by the anisotropic lattice distortion induced from the (011) plane of the PMN-PT substrate. This evidence shows that by utilizing our growth method, as illustrated in Fig. 1, moderate in-plane uniaxial magnetic anisotropy can be induced even in polycrystalline Co_2FeSi/PMN-PT(011) heterostructures. Because the (011) surface of the pseudo-cubic PMN-PT unit cell is distorted with shear strain along the red polarization vectors[46], we infer that the small deviation of the uniaxial easy axis from PMN-PT[01$\bar{1}$] is an intrinsic property of this system.

Strain-induced converse magnetoelectric effect

To characterize the electric field (*E*) effect on magnetic properties for the Co_2FeSi/PMN-PT(011) heterostructures, we perform magneto-optic Kerr ellipticity (η) measurements at room temperature by applying *E*, where *H* is applied to the crystallographic direction along PMN-PT[01$\bar{1}$] or [100] while *E* is applied to the PMN-PT[011] direction. Here, as a reference, the reported polarization switching process of a PMN-PT(011) single crystal is described in Fig. S4 of the Supplementary information[44]. Figure 3a shows the plots of the Kerr-ellipticity magnitude in the remanent state (η_R) as a function of *E* at room temperature, in which each point is obtained by measuring *H*-dependent Kerr-ellipticity curves along the PMN-PT[01$\bar{1}$] and PMN-PT[100] direction, as shown in Fig. 3b. Because we can clearly observe the saturation behavior of the Kerr-ellipticity magnitude (η_S) in Fig. 3b, we can assume that the value of η_S {$(611 \pm 3) \times 10^{-6}$ radian} corresponds to the value of M_S (1090 ± 30 kA/m) measured in Fig. 2b. On the basis of the assumption, the M_R values in the right axes in Fig. 3a are determined as $M_R = M_S$ (η_R/η_S).

Both $\eta_R - E$ curves shown in Fig. 3a indicate the presence of two magnetization states at $E = 0$. These features greatly differ from the conventional strain-induced magnetization vector switching processes that can be easily predicted from the polarization switching of PMN-PT(011), as shown in Fig. S4[21]. The appearance of the two magnetization states at

$E = 0$ is reproduced in multiple Co_2FeSi/PMN-PT(011) heterostructures, as shown in Fig. S5a of the Supplementary information[44]. To consider the origin of the two magnetization states at $E = 0$, we first refer to the general behavior of the lattice deformation of the (011) plane[21] after E is changed from 0 to ±0.8 MV/m and from ±0.8 MV/m to 0 in Fig. S4. When the large E of ±0.8 MV/m is applied (Fig. S4b, e), the long axis of the (011) rectangle plane is elongated along PMN-PT[01$\bar{1}$], and the short axis along PMN-PT[100] is simultaneously contracted. In contrast, when E is increased from −0.8 MV/m to 0 (Fig. S4c), the long axis along PMN-PT[01$\bar{1}$] is contracted, and the short axis along PMN-PT[100] is elongated. In this situation ($E = 0$), it is generally expected that the strain-induced magnetic easy axis of the Co_2FeSi film is aligned toward the PMN-PT[100] direction. However, the data presented in blue in Fig. 3b indicate that the PMN-PT[100] and PMN-PT[01$\bar{1}$] axes are magnetic hard and easy axes, respectively, in contrast to the simple expectation described above based on the reported polarization switching of the PMN-PT(011) substrate[21]. Thus, we next consider the presence of the anisotropic piezostrain at the PMN-PT(011) surface, as discussed in previous works on polycrystalline Ni/PMN-PT(011)[16] and amorphous CoFeB/PMN-PT(011)[28] systems.

In-plane piezostrain curves of the (011) surface of a representative PMN-PT(011) substrate are shown in Fig. S6 of the Supplementary information[44]. We clearly observed the anisotropic piezostrain of the (011) plane of the PMN-PT substrate between the PMN-PT[01$\bar{1}$] and PMN-PT[100] directions, as described in a previous report[28]. Because there were two different piezostrain states in the (011) plane between the PMN-PT[01$\bar{1}$] and PMN-PT [100] directions at $E = 0$ (Fig. S6c), we should consider the competition between the initial in-plane uniaxial magnetic anisotropy and the strain-induced magnetic anisotropy in the Co_2FeSi film at the two states. The two different states of the lattice deformation of the (011) plane at $E = 0$ are schematically shown in Fig. 3c, d. When E is increased from −0.8 MV/m to 0, the tensile strain along PMN-PT[01$\bar{1}$] is maintained at $E = 0$ (Fig. 3c). In this situation, the strain-induced uniaxial magnetic anisotropy of the Co_2FeSi film along the PMN-PT[01$\bar{1}$] direction is added to the initial uniaxial magnetic anisotropy along PMN-PT[01$\bar{1}$] with a small off-axis orientation. As a result, the magnetization direction of the Co_2FeSi film is maintained along a magnetic easy axis in the PMN-PT[01$\bar{1}$] direction. On the other hand, when E is decreased from +0.8 MV/m to 0, compressive strain along PMN-PT[01$\bar{1}$] is observed (Fig. 3d); this compressive strain decreases the magnitude of the uniaxial magnetic anisotropy of the Co_2FeSi film along the PMN-PT[01$\bar{1}$] direction. In this situation, the remanent magnetization direction of the Co_2FeSi film can switch from near the PMN-PT[01$\bar{1}$] to the PMN-PT[100] direction. Thus, we can qualitatively explain the origin of the two magnetization states at $E = 0$, shown in Fig. 3a, b, by considering the presence of the anisotropic piezostrain of the (011) surface of the PMN-PT substrate along the PMN-PT[01$\bar{1}$] direction at $E = 0$. However, if the initial in-plane uniaxial anisotropy of the Co_2FeSi film along the PMN-PT[01$\bar{1}$] direction was weaker or stronger than that in the present study, the two magnetization states at $E = 0$ could have been unstable. To quantitatively understand its origin, we should further investigate the correlation among the magnitude of the initial in-plane uniaxial magnetic anisotropy, local domain structures, and the magnitude of the global piezostrain[46,47] for many Co_2FeSi/PMN-PT(011) heterostructures at $E = 0$.

As shown in Fig. 3b, the magnetization directions at two different states at $E = 0$ are nearly switched from the uniaxial hard axis to the uniaxial easy axis or the uniaxial easy axis to the uniaxial hard axis during the E sweeping process. Therefore, nearly 90° magnetization vector switching can occur in the remanent state ($H = 0$) after the application of positive or negative E values, as schematically shown in Fig. 4a. Figure 4b, c display nonvolatile switching of the remanent magnetization vector for the measurements along the PMN-PT[01$\bar{1}$] and PMN-PT[100] directions, respectively, and the sequence of the E application to PMN-PT[011] is also displayed in Fig. 4d. Evident variations in two different magnetic states with high/low M_R can be repeatedly demonstrated for both measurements along the PMN-PT[01$\bar{1}$] (**b**) and PMN-PT[100] (**c**) directions. Notably, the observed variation in M_R was more than ~700 kA/m. The repeatable and nonvolatile magnetization vector switchings can be utilized as a part of the technology for voltage-induced magnetization switching in storage and/or memory devices having polycrystalline Co-based Heusler alloys.

Giant CME coupling coefficient

We quantitatively evaluate the CME effect of the Co_2FeSi/PMN-PT(011) heterostructures. To estimate the CME coupling coefficient (α_E), we define the value of α_E as follows: $\alpha_E = \mu_0 \frac{dM_R}{dE}$, where μ_0 is the vacuum permeability. Figure 5a displays the value of α_E as a function of E, estimated from the data in Fig. 3a, for the Co_2FeSi/PMN-PT(011) heterostructure in both measurements by applying H along the PMN-PT[01$\bar{1}$] and PMN-PT[100] directions. Very interestingly, the value of α_E was over 1.0×10^{-5} s/m when $E \sim -0.25$ MV/m at room temperature, as shown in Fig. 5a. In the relevant fields, an α_E of more than 1.0×10^{-5} s/m has thus far been reported in multiferroic heterostructures consisting of PMN-PT substrates and single-crystalline magnetostrictive materials such as FeRh[22] and FeGa alloys[34,35]. On the other hand, we observe the giant α_E of more than 1.0×10^{-5} s/m even in the polycrystalline Co_2FeSi/PMN-PT(011) heterostructure, where Co_2FeSi is one of the most

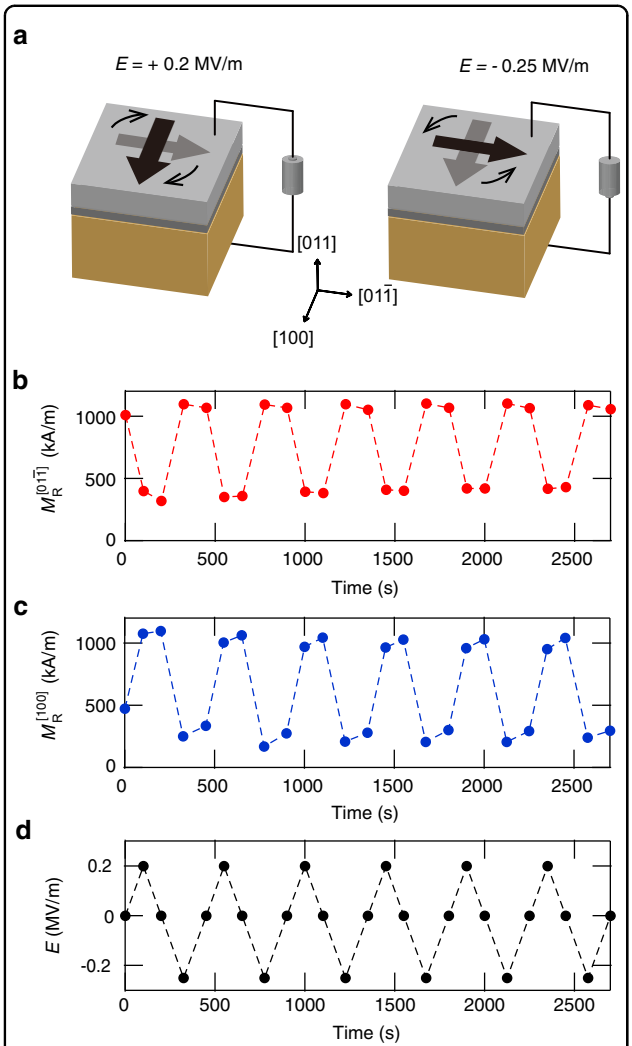

Fig. 4 Nonvolatile and repeatable switching of the magnetization vectors. a Magnetization vector switching by the application of *E*. **b**, **c** Repeatable switching of the remanent magnetization vector at room temperature for the measurements along the PMN-PT[01$\bar{1}$] and PMN-PT[100] directions, respectively. **d** The magnitude of *E* was applied with a bipolar sequence.

representative spintronic Co-based Heusler alloys[38,39]. This evidence indicates that magnetostrictive materials and single-crystalline structures are not strict conditions for obtaining a giant α_E of more than 1.0×10^{-5} s/m.

To verify the importance of Co_2FeSi, we also investigate the CME effect of the Fe_3Si/PMN-PT(011) heterostructure, where Fe_3Si is a binary Heusler alloy[42], and the growth of the heterostructure, including its characterizations, is also shown in Fig. S7 of the Supplementary information[44]. Here, the Fe_3Si/PMN-PT(011) heterostructure is also polycrystalline and shows an in-plane uniaxial magnetic anisotropy between the PMN-PT[01$\bar{1}$] and PMN-PT[100] directions, similar to the case of the Co_2FeSi/PMN-PT(011) heterostructures. Figure 5b shows the value of α_E as a function of *E* for the polycrystalline Fe_3Si/PMN-PT(011) heterostructure in both measurements along the PMN-PT[01$\bar{1}$] and PMN-PT[100] directions. Although similar peaks and dips are observed at $|E| \sim 0.20$ MV/m, α_E is relatively small compared to 1.0×10^{-5} s/m at room temperature. This feature is slightly different from that for the Co_2FeSi/PMN-PT(011) heterostructures.

In Table 1, we summarize the reported values of the giant α_E for various multiferroic heterostructures and compared them to those of this study. Apart from the $Fe_{50}Rh_{50}$/$BaTiO_3$(001) system[22], a giant CME effect was observed in various FM/PMN-PT systems[28,34,35]. As previously described, because ferroelectric PMN-PT has a piezoelectric constant[43] that is relatively large compared to that of $BaTiO_3$, a large piezostrain can be induced from PMN-PT to FM layers via multiferroic heterointerfaces[26–29,34,35]. For magnetostrictive materials such as $Fe_{1-x}Ga_x$, one has to achieve a metastable bcc (*A*2) phase with $x \sim 30\%$ as a single crystalline film on PMN-PT to obtain a giant α_E of more than 1.0×10^{-5} s/m[35]. For spintronic materials such as $Co_{40}Fe_{40}B_{20}$[28] and Co_2FeSi in this study, amorphous and polycrystalline films grown on PMN-PT have also shown giant values of α_E. Although these spintronic materials did not have a large magnetostrictive constant, an induced uniaxial magnetic anisotropy (6 kJ/m^3 for $Co_{40}Fe_{40}B_{20}$ in ref. [28], 5.8 kJ/m^3 for Co_2FeSi in this work) can be largely and steeply modulated in the film plane by applying *E*. The above results show that electric-field control of the magnetization vector can be efficiently achieved by utilizing the strain-mediated magnetic anisotropy for high-performance spintronic materials with a giant α_E.

Discussion

For the Co_2FeSi/PMN-PT(011) multiferroic heterostructures, we should consider the strain-mediated variation in the magnetic anisotropy, which is an extrinsic mechanism. To discuss a substantial contributor to the CME effect in the Co_2FeSi/PMN-PT(011) heterostructure, we focus on the correlation between the magnetocrystalline anisotropy energy for Co_2FeSi and the extrinsic lattice strain in Co_2FeSi in a simple model. Here, the extrinsic lattice strain is imposed through the in-plane lattice vectors *a* and *b* of the conventional 16-atom unit cell, as shown in the inset of Fig. 6a. Figure 6a shows the magnetocrystalline anisotropy energy (MAE) estimated by first-principles calculations for Co_2FeSi, together with Fe_3Si as a reference, as a function of *b*/*a*, where *b*/*a* is obtained by changing the lattice vector *a* while optimizing the *b* vector. The MAE of Co_2FeSi changes linearly with *b*/*a*, where the tetragonal in-plane lattice distortion results in in-plane magnetization pointing to the elongated axis: the positive and negative MAEs for $b/a > 1$ and $b/a < 1$, respectively. In contrast, Fe_3Si shows relatively small changes in the MAE with the opposite sign compared to Co_2FeSi. This tendency supports that the value of α_E for

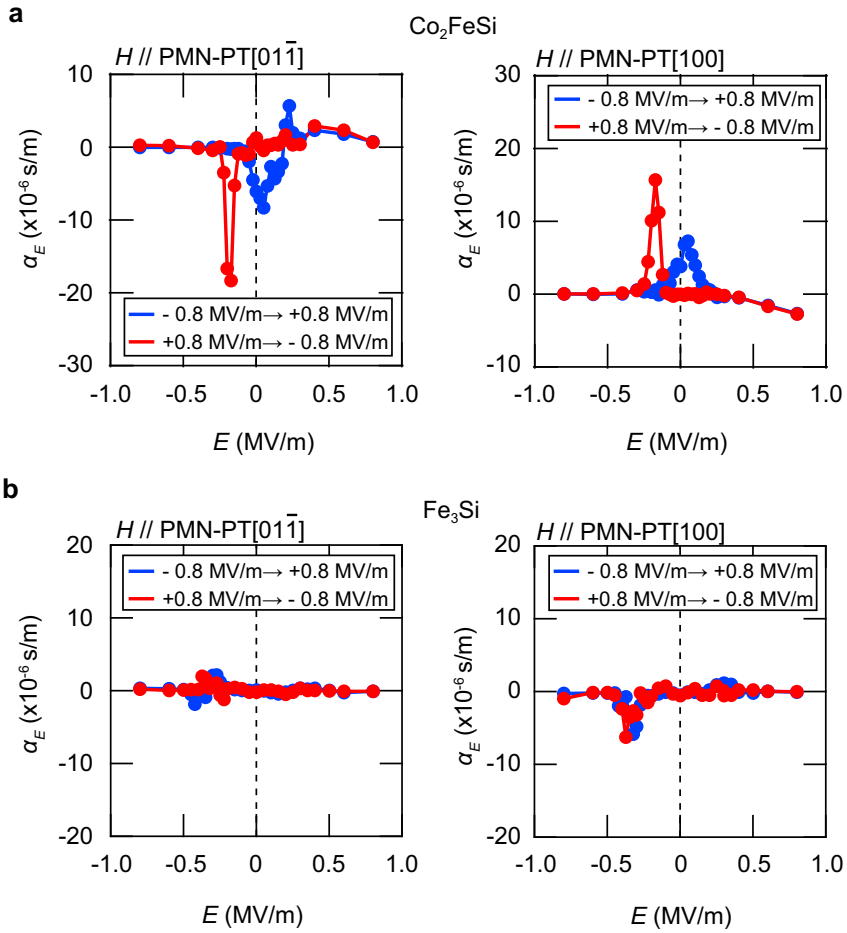

Fig. 5 Giant CME coupling coefficient. a Plots of the CME coupling coefficient (α_E) versus E at room temperature for the polycrystalline Co_2FeSi/PMN-PT(011) heterostructure along the PMN-PT[01$\bar{1}$] and PMN-PT[100] directions, where α_E is estimated from the data in Fig. 3a, **b** α_E versus E at room temperature for the polycrystalline Fe_3Si/PMN-PT(011) heterostructure along the PMN-PT[01$\bar{1}$] and PMN-PT[100] directions.

Table 1 Giant α_E for various multiferroic heterostructures.

Heterostructure	Crystal quality	α_E (s/m)	Temperature (K)	Reference
$Fe_{50}Rh_{50}/BaTiO_3(001)$	Single crystal	1.6×10^{-5}	385	[22]
$Fe_{80}Ga_{20}$/MgO/PMN-PT(001)	Single crystal	$1.5–4.5 \times 10^{-5}$	room temperature	[34]
$Fe_{70}Ga_{30}$/PMN-PT(001)	Single crystal	$1.5–2.0 \times 10^{-5}$	room temperature	[35]
$Co_{40}Fe_{40}B_{20}$/PMN-PT(011)	Amorphous	$3.0–8.0 \times 10^{-6}$	room temperature	[28]
Co_2FeSi/PMN-PT(011)	Polycrystalline	$1.2–1.8 \times 10^{-5}$	room temperature	This work

the Fe_3Si/PMN-PT(011) heterostructure is smaller than that for the Co_2FeSi/PMN-PT(011) heterostructure. From these results, we interpret that the modulation of the lattice strain induced by the application of E causes changes in the MAE in Co_2FeSi and Fe_3Si. Even though the result in Fig. 6a is obtained with the constraint of $c = a$ for simplicity, the behavior of the in-plane anisotropy favoring the magnetization along the elongated axis remains unchanged for the case of full relaxation, as shown in Fig. 6b.

To elucidate the origin of strain-induced MAE modulation, we evaluated the orbital-resolved MAE for Co_2FeSi on the basis of perturbation theory (see Materials and methods). As we decompose the total MAE of Co_2FeSi, it is found that the dominant contribution to the MAE comes from Co atoms relative to those from Fe and Si atoms.

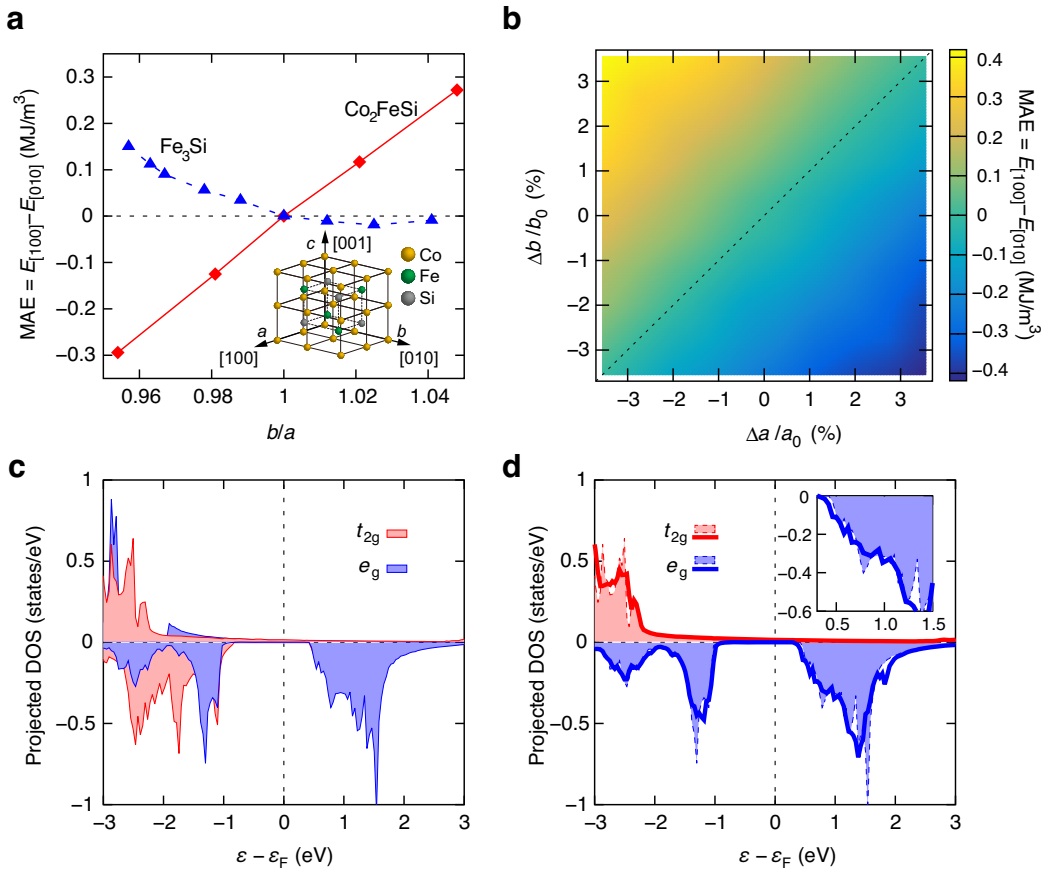

Fig. 6 Strain-induced modulation in magnetocrystalline anisotropy energy (MAE). a MAE of the Co_2FeSi and Fe_3Si as a function of *b*/*a*. **b** MAE of the Co_2FeSi as a function of the interfacial strain ($\Delta a/a_0$ and $\Delta b/b_0$). The dashed line represents the case of uniform in-plane deformation, where the MAE becomes exactly zero. **c** Projected DOS of Co 3*d* orbitals in Co_2FeSi without the strain. Relevant states (t_{2g} with up spins and e_g with down spins) for the strain-induced magnetic anisotropy are drawn as front. **d** Projected DOS per *d*-orbital of the dominant Co 3*d* states for the magnetic anisotropy in Co_2FeSi for $\Delta a/a_0 = 3.55\%$ and $\Delta b/b_0 = -3.55\%$. The case without strain is also shown as shades. In **a**, the ratio *b*/*a* is controlled by changing *a* while optimizing *b*, where *c* is fixed as *a* for simplicity. In contrast, vectors *a* and *b* were changed independently by optimizing *c* as the full relaxation for given strain states for **b**, **d**.

Figure 6c displays the projected density of states (DOS) of Co 3*d* orbitals in Co_2FeSi. Here, the e_g (t_{2g}) states consist of degenerate $d_{x^2-y^2}$ and $d_{3z^2-r^2}$ (d_{xy}, d_{xz}, d_{yz}) states because the octahedral ligand field is valid due to the cubic structure. Even though the degeneracy is lifted by the interfacial strain, we also use this classification for the strain-perturbed states. With lateral strain, we find that the MAE is dominated by up spins in the occupied states and down spins in the unoccupied states, in particular, $\langle t_{2g}, \uparrow | H_{SO} | e_g, \downarrow \rangle$ couplings, where the bra (ket) in the matrix element corresponds to occupied (unoccupied) states. These dominant orbitals are shown in Fig. 6d for $\Delta a/a_0 = 3.55\%$ and $\Delta b/b_0 = -3.55\%$. Subtle changes are seen from the DOS that the unoccupied e_g orbital with the down spins shifts toward the Fermi level (ε_F) by the in-plane deformation. The change in the electronic structures contributes to the negative MAE favoring the magnetization in the *a* direction. It should be noted that changes in the occupied down spins in Fig. 6d are irrelevant because the matrix element is small due to the very low density of states in unoccupied up-spin states. Therefore, the origin of the strain-induced MAE modulation in the Co_2FeSi/PMN-PT(011) heterostructures is related to the modulation of the Co-3*d* orbitals occupied by up-spin states in Co_2FeSi.

In the field of next-generation spintronic nonvolatile memories such as MRAMs[1–4] and spintronic logic devices[48,49], effective switching of the magnetization vector via spin transfer torque by using an electric current is one of the bottlenecks for low energy power consumption because of the heat dissipation process. In contrast, the CME effect in multiferroic heterostructures can provide a solution to overcome the heat dissipation of the magnetization switching at room temperature[23–25]. In this study, we have presented a giant CME effect in Co_2FeSi/PMN-PT(011) multiferroic heterostructures with α_E of more than 1.0×10^{-5} s/m at room temperature. The value of giant α_E is the

largest of the high-performance Heusler-based spintronic materials. We infer that the giant α_E in the Co_2FeSi/PMN-PT(011) heterostructures is strongly related to the strain-induced in-plane magnetic anisotropy derived from the Co 3*d* orbitals in Co_2FeSi, in addition to a relatively large M_S. Additionally, repeatable and nonvolatile magnetization vector switching without applying H has been demonstrated at room temperature. Thus, the present study provides a new solution for achieving magnetization switching with ultralow power consumption with hundreds of orders of magnitude of attoJoules in heat dissipation[23–25].

Although the present study was performed by utilizing PMN-PT substrates, some technologies for PMN-PT films without the influence of substrate clamping, such as piezoelectric layers, have been demonstrated[24,50]. Furthermore, the giant CME effect based on the Co-based Heusler alloys/PMN-PT multiferroic heterostructures can be utilized for MTJs[38,51] and current-perpendicular-to-plane giant magnetoresistance (CPP-GMR) devices with polycrystalline Co-based Heusler alloy electrodes[52] and a new spintronic logic architecture, such as magnetoelectric spin-orbit devices[23,53].

Materials and methods

Growth and characterization of Co_2FeSi on PMN-PT(011)

The Co_2FeSi/PMN-PT(011) multiferroic heterostructure was grown by molecular beam epitaxy (MBE). Prior to the growth of the Co_2FeSi film, heat treatment was performed at 450 °C for 20 min to obtain a flat surface of the single-crystal PMN-PT(011) substrates with a size of 5.0 × 5.0 × 0.5 mm^3. After cooling to a growth temperature of 300 °C, a 0.3-nm-thick Fe layer was grown on top of the cleaned PMN-PT(011) surface. When we did not use the 0.3-nm-thick Fe layer, the grown polycrystalline Co_2FeSi film became completely nonoriented. To improve the crystallinity of the Co_2FeSi film with an $L2_1$-ordered structure, the insertion of the 0.3-nm-thick Fe layer is essential. Thus, 30-nm-thick Co_2FeSi film was grown by co-evaporation using Knudsen cells, where we set the supplied atomic composition ratio of Co:Fe:Si to 2.0:1.0:1.0 during the growth[29,45]. Here, the heat treatment temperature of 450 °C and the growth temperature of 300 °C were lower than those described in the literature, showing a very high α_E of 1.5 − 4.5 × 10^{-5} s/m[34]. After growth, we characterized the Co_2FeSi/PMN-PT(011) multiferroic heterostructure. First, the multiferroic heterostructure was evaluated by X-ray diffraction (XRD) (Rigaku SmartLab) for out-of-plane and in-plane analyses. High-resolution transmission electron microscopy (HRTEM) and bright-field transmission electron microscopy (BF-TEM) were performed using an aberration-corrected JEOL 2200FS TEM, and nanobeam diffraction was performed on a JEOL 2100+TEM. The specimen preparation for TEM analysis was performed using focused ion beam techniques.

To measure the conventional magnetic properties of the grown multiferroic heterostructures, we used a vibrating sample magnetometer (VSM) at room temperature, while magneto-optic Kerr ellipticity measurements using the LED with a wavelength of 670 nm were performed to examine the CME effect at room temperature. To apply an E to the PMN-PT substrate along the [011] direction, a Au(100 nm)/Ti(3 nm) electrode was deposited on the backside of the PMN-PT substrate, where the Co_2FeSi film was also utilized as a top electrode. Prior to the evaluation of the CME effect, we first applied an E of −0.8 MV/m. Then, the amplitude of E was gradually changed from −0.8 MV/m to + 0.8 MV/m, then back to $E = -0.8$ MV/m. At each step, the Kerr-ellipticity magnitude was obtained by measuring the hysteresis loops as a function of H along the PMN-PT[01$\bar{1}$] or [100] direction.

Computational details for first-principles calculations

We performed first-principles calculations on the basis of density functional theory by using the VASP code[54], where the inner-core electrons were treated by the projector augmented-wave method[55,56]. The generalized gradient approximation parameterized by the Perdew-Burke-Ernzerhof functional was used for the exchange-correlation functional[57]. In addition, the DFT + U method with the effective Hubbard repulsion $U_{eff} = 2.6$ eV and $U_{eff} = 2.5$ eV was employed for the Co 3*d* and Fe 3*d* orbitals of Co_2FeSi, respectively[58]. The cutoff kinetic energy for the plane-wave basis set was set to 520 eV, and *k*-point grids were set to 10 × 10× 10 and 15 × 15× 15 for ionic relaxation and static calculations, respectively. The in-plane strain was generated by changing the in-plane lattice parameters a and b. Here, the strain was approximated with $\Delta a/a_0$ and $\Delta b/b_0$, where $\Delta a = a - a_0$, $\Delta b = b - b_0$, and a_0 (=b_0) is the equilibrium lattice constant without strain.

The MAE was evaluated as the total-energy difference obtained from calculations including the spin-orbit coupling for magnetization along the [100] and [010] directions while fixing the electron density that was obtained by the self-consistent collinear calculation. For the orbital-decomposed MAE, contributions from each atomic site τ and couplings among atomic orbitals μ were derived from second-order perturbation theory[59,60]:

$$E_{SO} = \sum_{\tau_1\tau_2}\sum_{\mu_1\mu_2} E_{SO}^{\tau_1\tau_2\mu_1\mu_2} \tag{1}$$

$$E_{SO}^{\tau_1\tau_2\mu_1\mu_2} \approx -\sum_{i}^{occ.}\sum_{j}^{unocc.}\sum_{\tau_3\tau_4}\sum_{\mu_3\mu_4}\frac{\langle i|\tau_1\mu_1\rangle\langle\tau_1\mu_1|H_{SO}|\tau_2\mu_2\rangle\langle\tau_2\mu_2|j\rangle\langle j|\tau_3\mu_3\rangle\langle\tau_3\mu_3|H_{SO}|\tau_4\mu_4\rangle\langle\tau_4\mu_4|i\rangle}{\varepsilon_j - \varepsilon_i} \tag{2}$$

where i and j are indices of occupied and unoccupied eigenstates with eigenenergies ε_i and ε_j, respectively. Note that the indices i, j, and μ include the spin index. The spin-orbit coupling is approximated as $H_{SO} = \xi l \cdot s$, where ξ is the coupling constant, l is the orbital-angular momentum quantum number, and s is the spin angular momentum quantum number. The values of ξ were compiled in a prior study[61]. In analyzing the MAE decomposition, electronic states obtained by the OpenMX code were used[62]. The x, y, and z directions in the MAE decomposition were defined as along the a, b, and c axes, respectively.

Acknowledgements
The authors appreciate Dr. Irene Azaceta of University of York for sample preparation related to TEM observations. This work was partly supported by JST CREST, Grant Number JPMJCR18J1, JSPS KAKENHI Grant Numbers 19H05616, 20K21002, 21K14196, and the Spintronics Research Network of Japan (Spin-RNJ). Some of the calculations were carried out on supercomputers at ISSP, The University of Tokyo, and TSUBAME, Tokyo Institute of Technology.

Author details
[1]Department of Systems Innovation, Graduate School of Engineering Science, Osaka University, 1-3 Machikaneyama, Toyonaka, Osaka 560-8531, Japan. [2]Center for Spintronics Research Network, Graduate School of Engineering Science, Osaka University, 1-3 Machikaneyama, Toyonaka, Osaka 560-8531, Japan. [3]Division of Materials and Manufacturing Science, Graduate School of Engineering, Osaka University, Suita, Osaka 565-0871, Japan. [4]Department of Physics, University of York, York YO10 5DD, United Kingdom. [5]Department of Materials Science and Engineering, Tokyo Institute of Technology, J1-3, Nagatsuta-cho 4259, Midori-ku, Yokohama 226-8502, Japan. [6]Division of Spintronics Research Network, Institute for Open and Transdisciplinary Research Initiatives, Osaka University, Suita, Osaka 565-0871, Japan

Author contributions
K.H. proposed and supervised this study. The growth of the ferromagnetic films was conducted by S.F., T.U., S.Y., and K.H. The XRD and HRTEM measurements were performed by S.F. and T.U. and by A.K. and V.L., respectively. The magnetic properties and the CME effect were characterized by S.F., T.U., Y.S., R.N., and K.H. The strain was measured by T.K. The theoretical calculations were carried out by A.Y. and Y.G., and the data analyses were performed by A.Y., Y.G., T.O. All authors contributed to the discussion and interpretation of the results and preparation of the manuscript.

Competing interests
The authors declare no competing interests.

Supplementary information The online version contains supplementary material available at https://doi.org/10.1038/s41427-022-00389-1.

Received: 9 November 2021 Revised: 26 March 2022 Accepted: 28 March 2022
Published online: 20 May 2022

References

1. Brataas, A., Kent, A. D. & Ohno, H. Current-induced torques in magnetic materials. *Nat. Mater.* **11**, 372 (2012).
2. Kent, A. D. & Worledge, D. C. A new spin on magnetic memories. *Nat. Nanotechnol.* **10**, 187–191 (2015).
3. Bhatti, S. et al. Spintronics based random access memory: a review. *Mater. Today* **20**, 530 (2017).
4. Yuasa, S., Hono, K., Hu, G. & Worledge, D. C. Materials for spin-transfer-torque magnetoresistive random-access memory. *MRS Bull.* **43**, 352–357 (2018).
5. Matsukura, F., Tokura, Y. & Ohno, H. Control of magnetism by electric fields. *Nat. Nanotechnol.* **10**, 209–220 (2015).
6. Chiba, D. et al. Magnetization vector manipulation by electric fields. *Nature* **455**, 515–518 (2008).
7. Yamada, Y. et al. Electrically induced ferromagnetism at room temperature in cobalt-doped titanium dioxide. *Science* **332**, 1065–1067 (2011).
8. Maruyama, T. et al. Large voltage-induced magnetic anisotropy change in a few atomic layers of iron. *Nat. Nanotechnol.* **4**, 158–161 (2009).
9. Nozaki, T. et al. Highly efficient voltage control of spin and enhanced interfacial perpendicular magnetic anisotropy in iridium-doped Fe/MgO magnetic tunnel junctions. *NPG Asia Mater.* **9**, e451 (2017).
10. Schmid, H. Multi-ferroic magnetoelectrics. *Ferroelectrics* **162**, 317 (1994).
11. Kimura, T. et al. Magnetic control of ferroelectric polarization. *Nature* **426**, 55–58 (2003).
12. Spaldin, N. A. & Fiebig, M. The Renaissance of Magnetoelectric Multiferroics. *Science* **309**, 391–392 (2005).
13. Spaldin, N. A. & Ramesh, R. Advances in magnetoelectric multiferroics. *Nat. Mater.* **18**, 203 (2019).
14. Duan, C. G., Jaswal, S. S. & Tsymbal, E. Y. Predicted magnetoelectric effect in Fe/$BaTiO_3$ multilayers: Ferroelectric control of magnetism. *Phys. Rev. Lett.* **97**, 047201 (2006).
15. Sahoo, S. et al. Ferroelectric control of magnetism in $BaTiO_3$/Fe heterostructures via interface strain coupling. *Phys. Rev. B* **76**, 092108 (2007).
16. Wu, T. et al. Electrical control of reversible and permanent magnetization reorientation for magnetoelectric memory devices. *Appl. Phys. Lett.* **98**, 262504 (2011).
17. Venkataiah, G., Shirahata, Y., Itoh, M. & Taniyama, T. Manipulation of magnetic coercivity of Fe film in Fe/$BaTiO_3$ heterostructure by electric field. *Appl. Phys. Lett.* **99**, 102506 (2011).
18. Venkataiah, G., Wada, E., Taniguchi, H., Itoh, M. & Taniyama, T. Electric-voltage control of magnetism in Fe/$BaTiO_3$ heterostructured multiferroics. *J. Appl. Phys.* **113**, 17C701 (2013).
19. Radaelli, G. et al. Electric control of magnetism at the Fe/$BaTiO_3$ interface. *Nat. Commun.* **5**, 3404 (2014).
20. Shirahata, Y. et al. Electric-field switching of perpendicularly magnetized multilayers. *NPG Asia Mater.* **7**, e198 (2015).
21. Zhang, S. et al. Giant electrical modulation of magnetization in $Co_{40}Fe_{40}B_{20}$/$Pb(Mg_{1/3}Nb_{2/3})_{0.7}Ti_{0.3}O_3$(011) heterostructure. *Sci. Rep.* **4**, 3727 (2014).
22. Cherifi, R. O. et al. Electric-field control of magnetic order above room temperature. *Nat. Mater.* **13**, 345–351 (2014).
23. Manipatruni, S. et al. Scalable energy-efficient magnetoelectric spin-orbit logic. *Nature* **565**, 35 (2019).
24. Hu, J.-M. & Nan, C.-W. Opportunities and challenges for magnetoelectric devices. *APL Mater.* **7**, 080905 (2019).
25. Hu, J.-M., Li, Z., Chen, L.-Q. & Nan, C.-W. High-density magnetoresistive random access memory operating at ultralow voltage at room temperature. *Nat. Commun.* **2**, 553 (2011).
26. Zhang, S. et al. Electric-field control of nonvolatile magnetization in $Co_{40}Fe_{40}B_{20}$/$Pb(Mg_{1/3}Nb_{2/3})_{0.7}Ti_{0.3}O_3$ structure at room temperature. *Phys. Rev. Lett.* **108**, 137203 (2012).
27. Zhang, S. et al. Strain-Mediated Coexistence of Volatile and Nonvolatile Converse Magnetoelectric Effects in Fe/$Pb(Mg_{1/3}Nb_{2/3})_{0.7}Ti_{0.3}O_3$ Heterostructure. *ACS Appl. Mater. Interfaces* **9**, 20637–20647 (2017).
28. Wang, J. et al. Giant non-volatile magnetoelectric effects via growth anisotropy in $Co_{40}Fe_{40}B_{20}$ films on PMN-PT substrates. *Appl. Phys. Lett.* **114**, 092401 (2019).
29. Usami, T. et al. Giant magnetoelectric effect in an $L2_1$-ordered Co_2FeSi/$Pb(Mg_{1/3}Nb_{2/3})O_3$-$PbTiO_3$ multiferroic heterostructure. *Appl. Phys. Lett.* **118**, 142402 (2021).
30. Liu, M. et al. Nonvolatile voltage-controlled magnetization reversal in a spin-valve multiferroic heterostructure. *NPG Asia Mater.* **13**, 64 (2021).
31. Chen, A. et al. Giant nonvolatile manipulation of magnetoresistance in magnetic tunnel junctions by electric fields via magnetoelectric coupling. *Nat. Commun.* **10**, 243 (2019).

32. Chen, A. et al. Full voltage manipulation of the resistance of a magnetic tunnel junction. *Sci. Adv.* **5**, eaay5141 (2019).
33. Biswas, A. K., Ahmad, H., Atulasimha, J. & Bandyopadhyay, S. Experimental Demonstration of Complete 180° Reversal of Magnetization in Isolated Co Nanomagnets on a PMN-PT Substrate with Voltage Generated Strain. *Nano Lett.* **17**, 3478–3484 (2017).
34. Begué, A. & Ciria, M. Strain-Mediated Giant Magnetoelectric Coupling in a Crystalline Multiferroic Heterostructure. *ACS Appl. Mater. Interfaces* **13**, 6778–6784 (2021).
35. Meisenheimer, P. B. et al. Engineering new limits to magnetostriction through metastability in iron-gallium alloys. *Nat. Commun.* **12**, 2757 (2021).
36. Wang, H. et al. Understanding strong magnetostriction in $Fe_{100-x}Ga_x$ alloys. *Sci. Rep.* **3**, 3521 (2013).
37. Yang, Z. et al. Scalable Nernst thermoelectric power using a coiled galfenol wire. *AIP Adv.* **7**, 095017 (2017).
38. Sakuraba, Y. et al. Giant tunneling magnetoresistance in Co_2MnSi/Al-O/Co_2MnSi magnetic tunnel junctions. *Appl. Phys. Lett.* **88**, 192508 (2006).
39. Felser, C., Fecher, G. H. & Balke, B. Spintronics: A challenge for materials science and solid-state chemistry. *Angew. Chem. Int. Ed.* **46**, 668 (2007).
40. Bombor, D. et al. Half-Metallic Ferromagnetism with Unexpectedly Small Spin Splitting in the Heusler Compound Co_2FeSi. *Phys. Rev. Lett.* **110**, 066601 (2013).
41. Kimura, T., Hashimoto, N., Yamada, S., Miyao, M. & Hamaya, K. Room-temperature generation of giant pure spin currents using epitaxial Co_2FeSi spin injectors. *NPG Asia Mater.* **4**, e9 (2012).
42. Hamaya, K. et al. Estimation of the spin polarization for Heusler-compound thin films by means of nonlocal spin-valve measurements: Comparison of Co_2FeSi and Fe_3Si. *Phys. Rev. B* **85**, 100404(R) (2012).
43. Guo, Y. et al. The phase transition sequence and the location of the morphotropic phase boundary region in (1-*x*)$[Pb(Mg_{1/3}Nb_{2/3})O_3]$- *x*$PbTiO_3$ single crystal. *J. Phys. Condens. Matter* **15**, L77 (2003).
44. See Supplementary information at [URL inserted by publisher] for XRD measurements for Co_2FeSi/Fe/PMN-PT(011) heterostructures, polarization switching process of PMN-PT(011), reproducibility of the giant CME effect, anisotropic piezoelectric response in the PMN-PT(011), and characterization of a Fe_3Si/PMN-PT(011) heterostructure.
45. Yamada, S. et al. Electric field tunable anisotropic magnetoresistance effect in an epitaxial $Co_2FeSi/BaTiO_3$ interfacial multiferroic system. *Phys. Rev. Mater.* **5**, 014412 (2021).
46. Ghidini, M. et al. Shear strain-mediated magnetoelectric effects revealed by imaging. *Nat. Mater.* **18**, 840–845 (2019).
47. Conte, R. L. et al. Influence of Nonuniform Micron-Scale Strain Distributions on the Electrical Reorientation of Magnetic Microstructures in a Composite Multiferroic Heterostructure. *Nano Lett.* **18**, 1952–1961 (2018).
48. Dery, H., Dalal, P., Cywiński, Ł. & Sham, L. J. Spin-based logic in semiconductors for reconfigurable large-scale circuits. *Nature* **447**, 573–576 (2007).
49. Behin-Aein, B., Datta, D., Salahuddin, S. & Datta, S. Proposal for an all-spin logic device with built-in memory. *Nat. Nanotechnol.* **5**, 266–270 (2010).
50. Irwin, J. et al. Magnetoelectric Coupling by Piezoelectric tensor Design. *Sci. Rep.* **9**, 19158 (2019).
51. Lim, W. C., Choi, G. M., Lee, T. D. & Seo, S. A. Fabrication of Magnetic Tunnel Junctions with Co_2FeSi Heusler Alloy and MgO Crystalline Barrier. *IEEE Trans. Magn.* **44**, 2595 (2008).
52. Nakatani, T., Li, S., Sakuraba, Y., Furubayashi, T. & Hono, K. Advanced CPP-GMR Spin-Valve Sensors for Narrow Reader Applications. *IEEE Trans. Magn.* **54**, 3300211 (2018).
53. Manipatruni, S., Nikonov, D. E. & Young, I. A. Beyond CMOS computing with spin and polarization. *Nat. Phys.* **14**, 338–343 (2018).
54. Kresse, G. & Furthmüller, J. Efficient iterative schemes for ab initio total-energy calculations using a plane-wave basis set. *Phys. Rev. B* **54**, 11169 (1996).
55. Blöchl, P. E. Projector augmented-wave method. *Phys. Rev. B* **50**, 17953 (1994).
56. Kresse, G. & Joubert, D. From ultrasoft pseudopotentials to the projector augmentedwave method. *Phys. Rev. B* **59**, 1758 (1999).
57. Perdew, J. P., Burke, K. & Ernzerhof, M. Generalized Gradient Approximation Made Simple. *Phys. Rev. Lett.* **77**, 3865 (1996).
58. Chen, J., Lin, C., Yang, Y., Hu, L. & Cheng, W. Ab initio study of the magnetoelectric effect and critical thickness for ferroelectricity in $Co_2FeSi/BaTiO_3$ multiferroic tunnel junctions. *Model. Simul. Mater. Sci. Eng.* **22**, 015008 (2014).
59. Nakamura, S. & Gohda, Y. Prediction of ferromagnetism in MnB and MnC on nonmagnetic transition-metal surfaces studied by first-principles calculations. *Phys. Rev. B* **96**, 245416 (2017).
60. Torbatian, Z., Ozaki, T., Tsuneyuki, S. & Gohda, Y. Strain effects on the magnetic anisotropy of $Y_2Fe_{14}B$ examined by first-principles calculations". *Appl. Phys. Lett.* **104**, 242403 (2014).
61. Yanase, Y. & Harima, H. Lecture on fundamental solid state physics: Spin-orbit interactions and electronic states in crystals (part 1). *Solid State Phys.* **46**, 229 (2011). [in Japanese].
62. Ozaki, T. Variationally optimized atomic orbitals for large-scale electronic structures. *Phys. Rev. B* **67**, 155108 (2003).